Data Engineering and Applications

Research Paper

State-Space Refinement Kalman Filter Model for Roadway Roof Deformation Detection in Underground LiDAR Scanning

Zainab Al-Zaabi[1], Hamdan Al-Suwaidi[1, *], Amal Al-Hashimi[2] and Mishaala Al-Tunaiji[2]

[1] College of Computing and Information Technology, Abu Dhabi University, Abu Dhabi, PO Box 59911, United Arab Emirates
[2] College of Engineering, Information Technology Division, University of Sharjah, Sharjah, PO Box 27272, United Arab Emirates
*Corresponding author: hamdan.su@adu.ac.ae

Abstract. In repeated underground laser scanning, road-roof deformation can be reliably determined through irregular sampling, support occlusion, registration drift, oblique incidence, and dust backscattering. In this paper, a state-space refined Kalman filter is developed, which integrates the following components: normal displacement, deformation rate, acceleration trend, registration bias, and local shape persistence. Without affecting field deployability, innovative statistics refined the delay estimation, fixed-lag backward smoothing refined the delay estimation, and robust patch correspondences generated roof-aligned observations. The experiment was conducted 18 times on a 2.4-kilometer-long road, including natural deformations and controlled roof offsets. Among the 36,720 roof patches evaluated, the proposed model reduced the root mean square error of the direct point-to-plane differential displacement from 8.7 mm to 3.4 mm, while the root mean square error of the traditional Kalman filter was reduced from 6.1 mm to Under a 10mm alarm threshold, the accuracy is 94.1%, the recall rate is 92.6%, and the false alarm rate is 2.8%. The processing time for each 20-meter segment at the standard workstation is 0.43 seconds, and the 95% uncertainty interval covers 94.7% of the reference observations. The ablation results indicate that innovative conditional covariance adaptation and bias state separation are the main contributors under dusty and low-overlap scanning conditions. Therefore, this model provides an interpretable and computationally feasible basis for the deformation screening of underground road operations.

Keywords: *Kalman Filtering, State-Space Modeling, LiDAR Point Clouds, Roof Deformation, Adaptive Covariance*

Received on 17 October 2022, Accepted on 29 December 2022, Published on 24 January 2023

Introduction

Underground roadway roofs have experienced changes in stress distribution, blasting damage, water softening and progressive separation along the bedding. Small vertical displacements can occur before open cracks, but the standard convergence station sampling locations are relatively few and may require personnel to enter the disturbed area. Mobile laser scanning switches to a high-density surface geometry collection mode for long-range headings. However, the apparent density should not be taken as a metrological value; many factors influence the reconstructed surface, such as the angle of incidence, reflectance, airborne dust, wet rock, mesh, bolts and vehicle motion [1]. Therefore, repeated point clouds contain both structural motion and sensing artifacts [2]. A high-quality filter needs to remove the displacement signal's displacement without smoothing the local sag [3]. The previous point-to-point comparisons are still affected by sampling mismatch [4]. Surface fitting improves repeatability but blurs discontinuities [5]. The Quality of registration is relatively poor at a deformation of a few mm [6].

By studying underground 3D maps, simultaneous localization and loop closure, as well as geometric reconstruction, have been improved, making repeated surveys more feasible [7]. Common change detection methods include roof segmentation, local normal estimation, threshold processing, and registration periods [8]. Robust correspondence, multi-scale descriptors and probabilistic occupancy models reduce some outliers [9].

Most pipelines treat each pair of epochs independently, fail to consider that roof motion is temporally correlated, and show varying survey quality across passes [10]. Traditional Kalman filtering assumes temporal continuity and uses a fixed noise model; thus, it cannot account for the strong heteroscedasticity induced by angle, point density, dust, and incomplete overlap [11]. An unmodeled registration bias can also be treated as deformation and remains in many adjacent patches [12]. The resulting alarms may be spatially correlated and therefore deceptively plausible.

This paper addresses the problem mentioned above by designing a state-space refinement Kalman filter for the error characteristics of underground LiDAR. The state is divided into normal roof displacement and its rate, acceleration tendency, scan-level registration bias, and a local shape-persistence term. Set up observations in a roof-aligned coordinate system, weight them according to patch geometry, and filter through a robust innovation gate. According to recent standardized innovations and scanning evidence, measuring covariance is coordinated with lagged observations through fixed lags. A physically intuitive model, a deployable processing workflow, and a patch-level uncertainty measure that supports threshold-based decisions are provided in this paper. Evaluate the accuracy, alarms, calibration, robustness and runtime of controlled offset and operational road scan data, etc., in addition to mean distance error.

Related Work

LiDAR-Based Underground Deformation Measurement

Repeatedly carried out terrestrial and mobile laser scanning, these methods are now commonly used to record the geometry of tunnels and excavation damage and convergence beyond what sparse extensometers can achieve [13]. Cloud-to-cloud and cloud-to-mesh distances are straightforward, but their sign and magnitude depend on local sampling and the selected reference surface [14]. For roofs with ribs, grids, and bolt plates, it is difficult to determine the confidence limits of surface changes using inter-scale model comparisons [15]. Cross-sectional fitting is suitable for regular tunnels, but mine roadways often deviate significantly from an ideal ellipse [16]. Feature-based registration improves the global alignment of long corridors but loses constraints in repetitive roof regions [17]. Recently, semantic segmentation methods have removed machinery and support facilities, but their transfer between mines is still affected by scanners and geology [18].

State Estimation and Robust Temporal Filtering

A state estimator can help integrate the noisy data from several sources conveniently. Linear Kalman filters are computationally convenient, but their performance is affected by process and measurement covariance that are rarely stationary in field sensing [19]. Adaptive Covariance Methods adaptively adjust to changes in noise based on residual statistics; otherwise, unrestricted adaptation may be unstable after an outlier [20]. Robust filters are used to limit the impact of a single contaminated measurement by restricting its influence through bounded influence or mixture likelihoods and gating [21]. Smoothing methods use future observations to improve a past estimate and are suitable for monitoring decisions that can tolerate a short delay [22]. Latent bias states in geometric monitoring can distinguish sensor drift from structural response, but observability must be supported by spatial anchors or scan-quality evidence [23]. No well-known formulation combines roof-normal geometry, scan-level bias separation, constrained covariance adaptation and fixed-lag refinement for dense underground LiDAR deformation screening.

Roof-Aligned Observation Construction

Coordinate Conditioning and Patch Correspondence

All scans are converted to the road coordinate system and aligned along the longitudinal centerline of the survey. By using the minimum bounding box to move along the centerline, the roll of the scanner and the curvature of the centerline do not produce artificial normal variations between different time periods. The roof band is identified by height, surface orientation, intensity discontinuity and local planarity. Bolt plates, mesh edges, pipes and transient vehicle returns are only retained as low-confidence candidates and are not allowed to define the roof surface. The reference roof is divided into overlapping $0.40\ \mathrm{m} \times 0.40\ \mathrm{m}$ patches with a 0.20m stride, and a scale is used that keeps the local sag but provides enough points for stable plane fitting.

$$r_{ij,k} = \boldsymbol{n}_i^{\top}(\boldsymbol{p}_{j,k} - \boldsymbol{c}_i) \qquad \text{Eq.(1)}$$

For reference patch i, a trimmed covariance estimates supplies centroid $\mathbf{c}_i$ and unit normal $\mathbf{n}_i$ directed toward the roadway void. Candidate points from epoch k are searched inside an elliptical neighborhood and must satisfy limits on centroid offset, normal difference, and overlap. Their signed normal residuals are calculated before robust aggregation. The roof-aligned projection measures displacement in the direction of structural support and does not mix tangential sampling offsets with vertical displacement.

$$z_{i,k} = \underset{j}{median}\{r_{ij,k}: |r_{ij,k}| \le \tau_{i,k}\} \qquad \text{Eq.(2)}$$

Patch observation is the median of the accepted signed residuals. Median aggregation is used because the dust returns and mesh reflections are sparse, but they can be several times larger than the deformation of interest. Missing or geometrically degenerate patches are still marked as missing observations and are not spatially interpolated prior to filtering. Thus, the process returns an observed normal displacement and its geometric indicators, rather than a pre-corrected surface.

Quality-Weighted Observation and Gating

The Confidence of observation changes in an underground scan. A Huber weight is assigned to each projected residual according to the robust patch scale $s_{i,k}$ and a tuning constant δ. Residuals in the central range are given a weight of one, and increasingly inconsistent returns are boundedly influenced. The effective sample size is the product of the number of points and their unequal reliabilities; a dense but narrow footprint cannot be more informative than a well-distributed patch.

$$w_{ij,k} = min\left(1, \frac{\delta s_{i,k}}{|r_{ij,k} - z_{i,k}|}\right) \qquad \text{Eq.(3)}$$

The initial measurement covariance is estimated based on an observable quality vector $\mathbf{q}_{i,k}$ that includes incidence angle, effective point count, overlap, surface roughness, intensity dispersion and trajectory residual. A non-negative coefficient will not reduce the predicted variance for a worse geometry. Point-count benefit saturates after full coverage, and low overlap and high incidence incur an explicit penalty. The covariance must be in a physically reasonable range of 1-20 mm for the standard deviation.

$$R_{i,k}^{0} = \frac{\sigma_0^2 exp(\boldsymbol{\beta}^{\top}\boldsymbol{q}_{i,k})}{N_{i,k}^{eff}} \qquad \text{Eq.(4)}$$

Quality Weighting is performed prior to the examination of temporal innovation. The two are not the same: Geometry is about how reliable the current scan should be, and innovation later checks whether that prediction matches the state history. Patches with less than 35% overlap or those that are only line-like point supports are considered weak and provide little support, only increasing the covariance. Thus, no spurious precision is added to the inadequately observed area of the roof.

Registration Anchors and Bias Evidence

Stable sidewall and floor regions provide independent evidence of scan-level registration bias. Their normal residuals are combined by quality weights to obtain the bias observation. The value is passed to the state estimator with its uncertainty instead of being subtracted as an exact correction. At least three spatially distributed anchor regions are required; otherwise, the segment remains processable but receives a low-observability flag.

$$\tilde{b}_k = \frac{\sum_{a\in\mathcal{A}} \omega_{a,k}\boldsymbol{n}_a^{\top}\Delta\boldsymbol{p}_{a,k}}{\sum_{a\in\mathcal{A}} \omega_{a,k}} \qquad \text{Eq.(5)}$$

Anchor Selection is independent of the estimated roof deformation. The candidate region should have good local planarity, sufficient point density, and repeated visibility over several epochs. Areas near floor heave, sidewall spalling, drainage channels, moving equipment or recently installed services should be excluded from the calculation because their displacement is not assumed to be negligible. The other two anchors are at the beginning and end of the path where the road geometry allows. Distribution in Space can help distinguish

https://doi.org/10.64972/dea.2023.v2i1.2942d:16-27

translational drift from small rotational misalignment; otherwise, a systematic displacement gradient would occur across the roof.

The uncertainty of the bias observation is derived from the weighted dispersion of anchor residuals and the spatial leverage of anchor arrangement. Consistent anchors have a small bias interval, and disagreement among the anchor group increases the uncertainty of the value before it enters the filter. A single high-confidence anchor should not be allowed to dominate the segment estimation. If the anchor residuals form two incompatible clusters, the scan is labelled as geometrically ambiguous and the roof patches receive prediction-only or strongly down-weighted updates. The above conservative measures will prevent damage to a small area or partial trajectory deviation from developing into a widespread roof deformation.

Figure 1 is the observation path from trajectory conditioning and support-aware roof extraction to patch correspondence, quality encoding, and anchor evidence. Roof patches determine the local displacement channel, and sidewall and floor anchors constrain the shared bias channel. The two channels meet only in the Kalman update, and thus uncertain registration evidence is not counted twice.

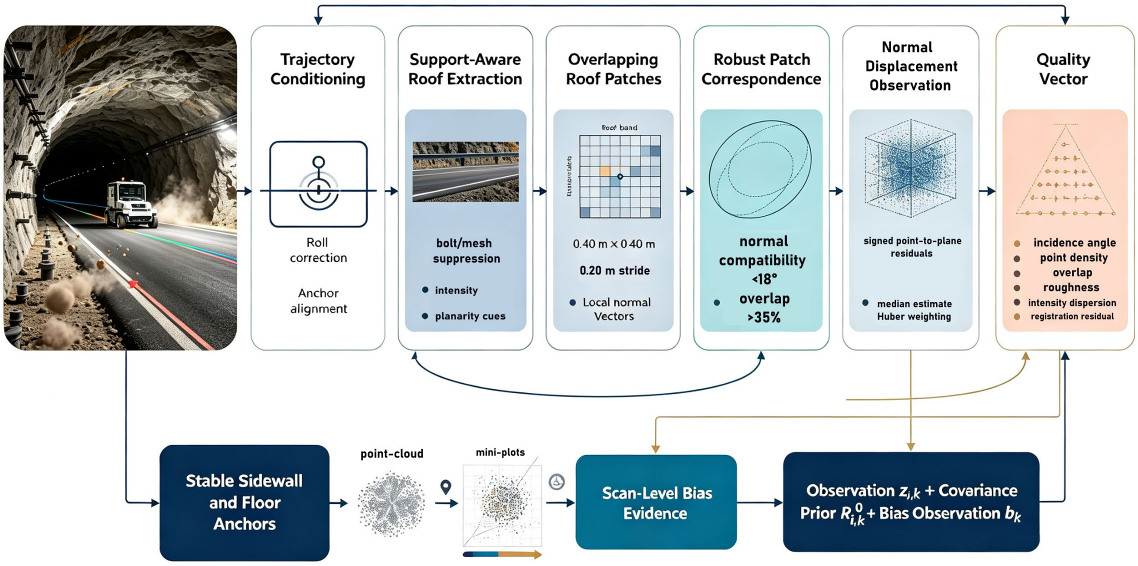

Figure 1. Roof-aligned observation construction.

State-Space Refinement Kalman Filter

Augmented Dynamic Model

For each roof patch, the augmented state includes normal displacement, deformation velocity, acceleration tendency, a segment-shared registration bias, and a local shape-persistence term. The end state is a slow recurrence of mismatch caused by rough rock and would otherwise be absorbed by displacement. A constant-acceleration block drives the motion of the structure, and bias and persistence are damped random walks. Based on the actual time elapsed since the last campaign, the transition matrix will be set rather than according to a fixed survey cycle.

$$\boldsymbol{x}_{i,k} = [d_{i,k} \quad v_{i,k} \quad a_{i,k} \quad b_k \quad h_{i,k}]^\top \qquad \text{Eq.(6)}$$

Process covariance is in physical units and scaled by the time elapsed. Blasting or excavation records can temporarily increase the acceleration spectral density; poor scan geometry only affects measurement covariance. The above mechanisms are not prone to false alarms caused by a noisy survey. Covariance eigenvalues are bounded to prevent numerical collapse or unbounded state drift.

$$\boldsymbol{x}_{i,k} = \boldsymbol{F}(\Delta t_k)\boldsymbol{x}_{i,k-1} + \boldsymbol{w}_{i,k}, \boldsymbol{w}_{i,k} \sim \mathcal{N}\left(\boldsymbol{0}, \boldsymbol{Q}_{i,k}\right) \qquad \text{Eq.(7)}$$

Roof observations alone can only identify a combination of displacement, bias and persistence. Observability is provided by the anchor measurement, temporal damping of persistence, and repeated dynamic coupling among

https://doi.org/10.64972/dea.2023.v2i1.2942d:16-27

displacement, velocity, and acceleration. Calculate the windowed condition measure for each section. Anchors are sparse; therefore, nuisance-state uncertainty is high and an alarm is not triggered due to minor deviations.

$$\boldsymbol{P}_{i,k}^{-} = \boldsymbol{F}\boldsymbol{P}_{i,k-1}^{+}\boldsymbol{F}^{\top} + \boldsymbol{Q}_{i,k} \quad \text{Eq.(8)}$$

Initialization uses the first two available valid campaigns. Displacement is the difference of the two, velocity is its change over time, acceleration is zero, and all have large uncertainties. Anchors are used to initialize bias, and reference roughness is saved as persistence. When prolonged occlusion or coordinate system changes are detected, the patch will be reinitialized.

Innovation-Conditioned Robust Update

The evidence of deviation derived from the normal displacement of the roof and the anchor point constitutes the observation vector. The geometric condition values in Section 3.2 are the first measurement covariance. Subsequently, the difference between the predicted state and the current scan is calculated using the innovation and its covariance. Check the residuals of the roof and anchor point channels to determine local deformations or alignment offsets of the entire segment.

$$\boldsymbol{y}_{i,k} = \boldsymbol{z}_{i,k} - \boldsymbol{H}\boldsymbol{x}_{i,k}^{-}, \boldsymbol{S}_{i,k} = \boldsymbol{H}\boldsymbol{P}_{i,k}^{-}\boldsymbol{H}^{\top} + \boldsymbol{R}_{i,k} \quad \text{Eq.(9)}$$

Normalize the innovation squared and compare with chi-square limits. Measurements in the accepted region use the ordinary update. Values in a soft region are smoothed by a bounded Huber function, and outliers are excluded; only prediction-only propagation occurs. A large roof innovation with normal anchors indicates a local change or local contamination; a simultaneous roof and anchor innovation indicates registration degradation.

$$\eta_{i,k} = \boldsymbol{y}_{i,k}^{\top}\boldsymbol{S}_{i,k}^{-1}\boldsymbol{y}_{i,k} \quad \text{Eq.(10)}$$

Covariance adaptation uses exponential forgetting and is constrained by geometry-dependent lower and upper bounds. The innovation outer product addresses the slow mismatch in predicted and observed dispersion, but a single corrupted scan cannot change the noise model. Adaptation is not performed for rejected observations, and it is limited when fewer than half of the segment patches are still valid.

$$\boldsymbol{R}_{i,k} = clip\left[(1-\lambda)\boldsymbol{R}_{i,k-1} + \lambda\left(\boldsymbol{y}_{i,k}\boldsymbol{y}_{i,k}^{\top} - \boldsymbol{H}\boldsymbol{P}_{i,k}^{-}\boldsymbol{H}^{\top}\right)\right] \quad \text{Eq.(11)}$$

The robust Kalman gain is calculated with the reweighted covariance. The posterior covariance uses the Joseph stabilized form, is explicitly symmetrized, and receives a small eigenvalue floor. These safeguards are inexpensive for the five-state system and prevent isolated numerical failures from creating extreme deformation alarms in long roadways.

$$\boldsymbol{K}_{i,k} = \boldsymbol{P}_{i,k}^{-}\boldsymbol{H}^{\top}\left(\boldsymbol{H}\boldsymbol{P}_{i,k}^{-}\boldsymbol{H}^{\top} + \widetilde{\boldsymbol{R}}_{i,k}\right)^{-1} \quad \text{Eq.(12)}$$

Spatial consistency is applied after the measurement update through an anisotropic patch graph. On surfaces with consistent normal directions, the connections are very strong, but weak on ribs, support boundaries, and curvature ridges. The operator only reduces the high-frequency residuals of the robust neighborhood trend and increases the associated regularization uncertainty. Coherent deformation clusters therefore remain sharp, while unsupported single-patch spikes are attenuated.

Process and measurement diagnostics are retained separately. Innovation categories, covariance adaptation ratio, bias trajectory, rejected patch ratio, and neighborhood correction are part of the stored data. They support audit and maintenance without being blended into an opaque alarm score.

Fixed-Lag Refinement and Alarm Logic

After completing the quality control of the new task, the last four stages undergo reverse optimization. The stored predictions and filtering moments provide a refinement gain, which will be mapped back to the next refinement state correction. Compared to displacement corrections, corrections for bias and persistence are subject to stricter limitations. Therefore, subsequent registration anomalies will not overwrite early structural information.

$$\boldsymbol{G}_{i,k} = \boldsymbol{P}_{i,k}^{+}\boldsymbol{F}^{\top}\left(\boldsymbol{P}_{i,k+1}^{-}\right)^{-1} \quad \text{Eq.(13)}$$

When most observations are rejected in a segment, the smoothed covariance allows the model to be mismatched with the smoother. With a delay of four cycles, the noise will be reduced to a lower level. The forward state now issues high-probability alerts, with no further refinement, and the previous estimates remain unchanged.

$$\boldsymbol{x}_{i,k}^{r} = \boldsymbol{x}_{i,k}^{+} + \boldsymbol{G}_{i,k}\left(\boldsymbol{x}_{i,k+1}^{r} - \boldsymbol{x}_{i,k+1}^{-}\right) \qquad \text{Eq.(14)}$$

Alarm logic combines displacement exceedance probability, deformation rate, and spatial support. A patch enters watch status when the probability of exceeding 10 mm is greater than 0.80 and at least two neighbors move compatibly. It becomes an alert when probability exceeds 0.95 or the estimated rate remains above 2.5 mm per campaign for two epochs. Hysteresis prevents status chatter, and a missing scan cannot clear an existing alert.

Figure 2 links prediction, geometry-conditioned covariance, robust innovation handling, neighborhood control, fixed-lag refinement, and alarm output. The system stores both forward and refined estimates, uncertainty intervals, gate states, and contributing neighbors, providing a traceable basis for engineering review.

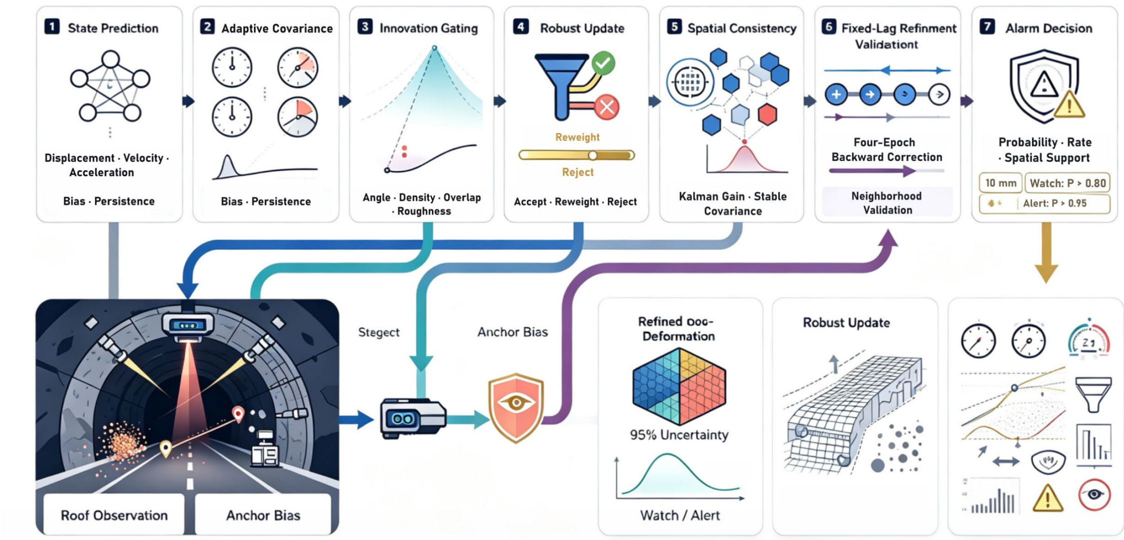

Figure 2. State-space refinement workflow.

Experimental Evaluation

Data, Protocol, and Baselines

The evaluation comprised 18 scanning campaigns along 2.4 km of active coal-mine roadway. Twelve 20 m-controlled sections contained rigid roof targets displaced by 0, 3, 5, 8, 10, 15, and 25 mm using calibrated spacers; six operational sections contributed naturally changing roof surfaces checked by total-station prisms and manual convergence points. The scanner produced 300,000 points per second, and survey speed ranged from 0.7 to 1.2 m/s. After quality screening, 36,720 patch-epoch observations remained. Dust concentration, mean incidence angle, overlap, and support density were retained as covariates. Reference uncertainty was 1.2 mm for controlled targets and 2.0 mm for operational checks.

Baselines include direct point-to-plane differencing, multiscale cloud comparison, robust local plane change, a conventional constant-velocity Kalman filter, and an adaptive filter without an explicit bias state. Tune the parameters of the four controlled sections and then freeze them for evaluation. The selected indicators are root mean square error, median absolute error, 95th-percentile error, precision, recall, F1 score, false alarm rate, interval coverage, negative log-likelihood and runtime. Bootstrap confidence intervals used roadway section as the resampling unit. The evaluation protocol will be in line with current practices for spatial change detection, and all cited methods will be represented by placeholders [24]. Scanner calibration was verified before every campaign [25]. Ground-control stability was independently confirmed [26].

Controlled offsets were installed before scanning and concealed from the processing operator. Each campaign was registered using the same anchor policy, and no manual correction was allowed after deformation maps were viewed. A patch was matched to a target only when at least 60% of its footprint lay inside the target region.

Operational reference points were interpolated only along the local roof normal and were excluded if prism visibility was interrupted. These restrictions reduced the available sample but prevented ambiguous ground truth. In order to maintain the spatial correlation between patches within the road segment, 2,000 segmented bootstrap resampling were used to calculate the confidence interval.

The purpose of selecting hyperparameters is to reduce the overall tuning loss, including false positives, insufficient interval coverage, and displacement errors. Preheat tests were conducted on an eight-core workstation with 32GB of memory, and then the runtime was recorded. In applicable cases, all methods received the same conditional point cloud and correspondences. Therefore, the differences are due to estimation rather than preprocessing. The suggested neighborhood size is used for direct and multi-scale baselines, while traditional filters are independently adjusted rather than using process covariance. Missing observations are considered missing in the time method and then excluded from the paired method.

Accuracy, Robustness, and Calibration

Figure 3(a) compares displacement errors across six methods: root-mean-square error decreased from 8.7 mm for direct differencing, 7.3 mm for multiscale comparison, 6.8 mm for robust plane change, 6.1 mm for the conventional filter, and 4.5 mm for adaptive filtering to 3.4 mm for the proposed model. Figure 3(b) shows threshold behavior; at 10 mm, precision was 94.1%, recall was 92.6%, and F1 was 93.3%, while the false-alarm rate remained 2.8%. The strongest gain occurred between 8 and 15 mm, where raw distance fields often confused registration drift with roof movement. The comparison uses section-level testing to avoid optimistic patch leakage [27].

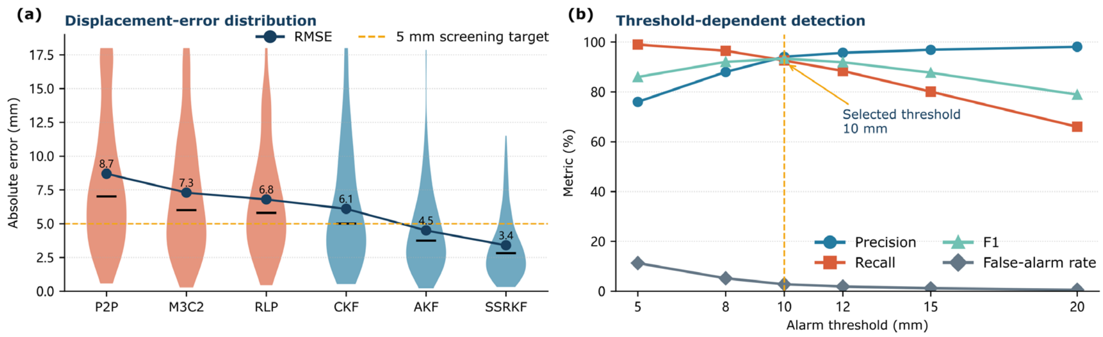

Figure 3. Overall detection performance: (a) displacement-error distributions and summary metrics for six methods; (b) precision, recall, F1 score, and false-alarm rate across alarm thresholds.

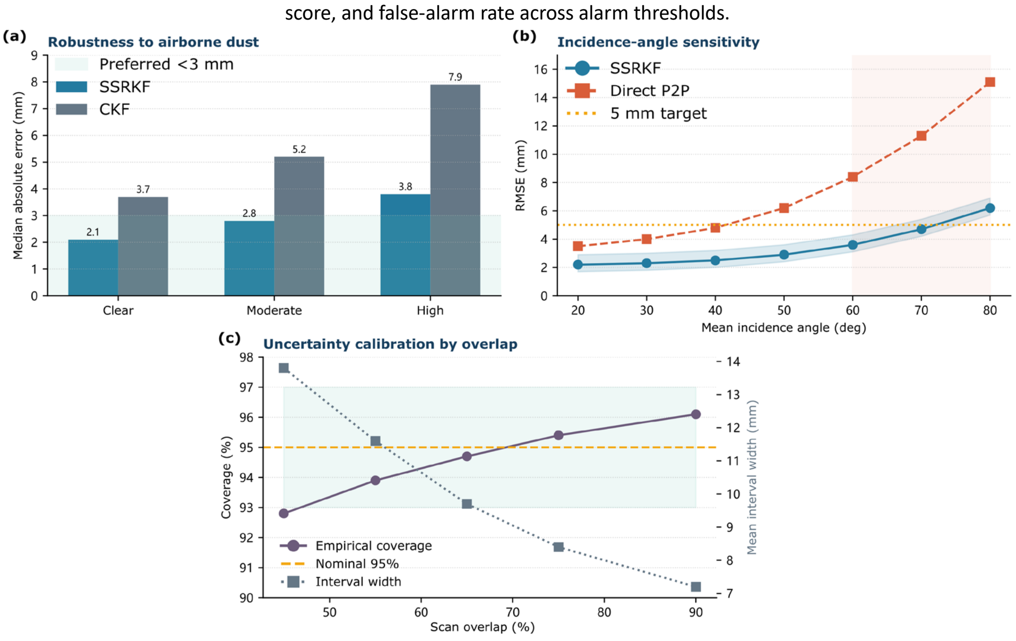

Figure 4. Environmental robustness: (a) error by dust level; (b) error versus incidence angle; (c) uncertainty coverage across scan-overlap bins.

Environmental stratification is reported in Figure 4. In Figure 4(a), median absolute error rose from 2.1 mm in clear air to 3.8 mm under high dust, compared with 3.7 to 7.9 mm for the conventional filter. Figure 4(b) plots error against incidence angle: the proposed curve stayed below 5 mm through 70 degrees, whereas direct differencing exceeded 10 mm beyond 60 degrees. Figure 4(c) shows that 95% interval coverage remained between 92.8% and 96.1% across overlap bins from 45% to 90%. These results support covariance adaptation based on observable scan conditions rather than a single fixed noise value [28].

Figure 5(a) maps a 60 m roadway segment and locates two coherent sag zones at 18–24 m and 46–50 m, with peak refined displacements of 17.6 and 12.4 mm. Figure 5(b) shows epoch trajectories for four representative patches; the alerting patch increased from 4.2 to 17.6 mm over six campaigns while a nearby stable patch remained within plus or minus 2.3 mm. Figure 5(c) presents the innovation distribution, where robust gating reduced the heavy positive tail and retained 91.5% of measurements as full updates. Figure 5(d) contrasts forward and refined estimates: refinement reduced median absolute error from 3.0 to 2.4 mm without delaying alerts by more than one campaign. Similar uncertainty reporting has been recommended for operational monitoring [29].

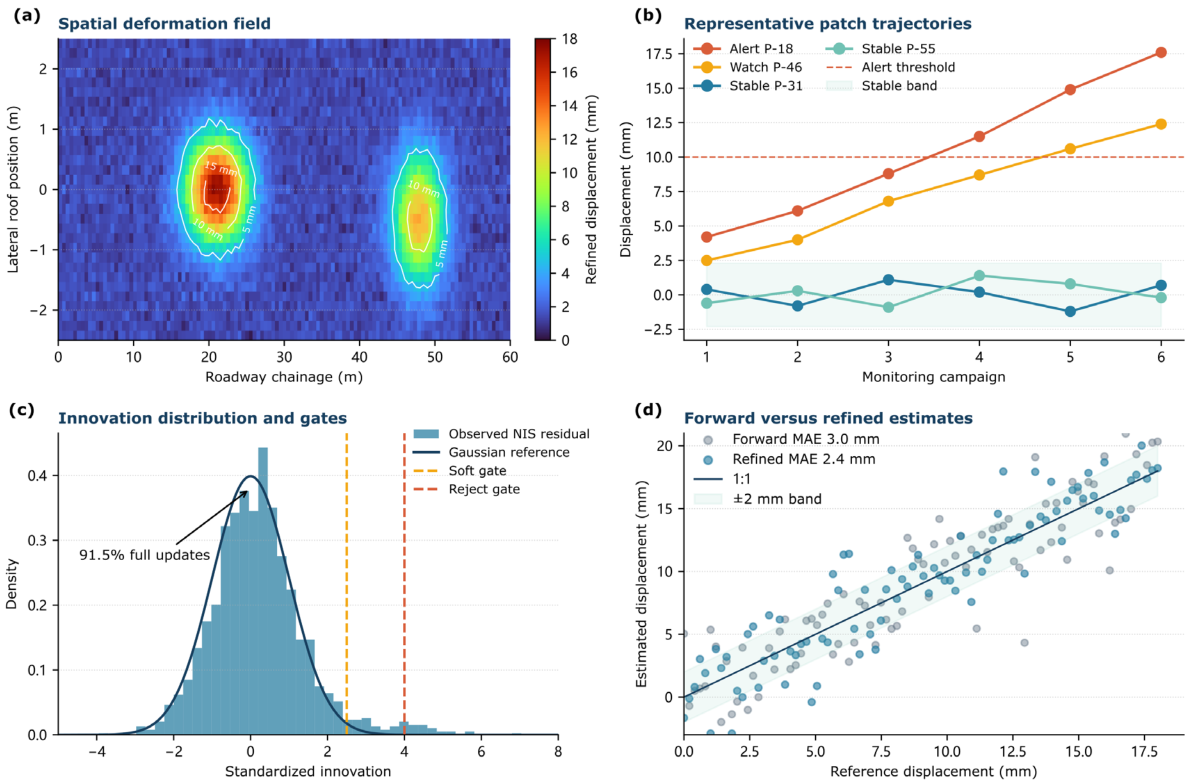

Figure 5. Spatial and temporal behavior: (a) roadway deformation map; (b) representative patch trajectories; (c) normalized-innovation distribution and gating regions; (d) forward versus fixed-lag refined estimates.

Ablation results appear in Figure 6. Figure 6(a) shows that removing bias separation increased root-mean-square error from 3.4 to 4.8 mm, removing adaptive covariance raised it to 4.5 mm, removing backward refinement raised it to 4.0 mm, and removing neighborhood control raised it to 3.9 mm. Figure 6(b) decomposes false alarms: bias separation removed 41% of registration-driven alarms, while robust gating removed 34% of dust-driven alarms. The contributions are not additive because poor registration and dust often co-occur. Ablation settings retained identical thresholds and test sections [30].

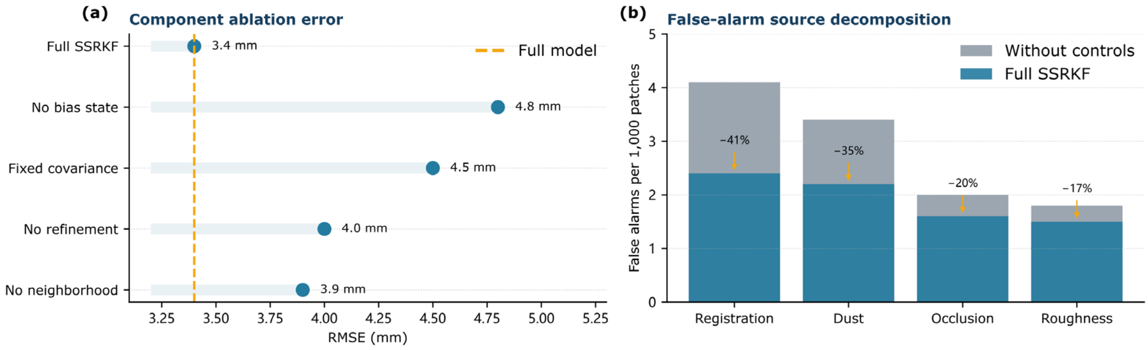

Figure 6. Component ablation: (a) error metrics after removing each model component; (b) false-alarm causes and reductions attributed to bias separation and robust gating.

Figure 7(a) reports runtime by segment length; total processing was 0.43 s per 20 m and 1.91 s per 100 m, with correspondence search accounting for 46% of cost. Figure 7(b) shows memory usage increasing from 0.38 GB at 20 m to 1.26 GB at 100 m. Figure 7(c) indicates stable accuracy for patch widths from 0.30 to 0.50 m, with the minimum error at 0.40 m. Figure 7(d) plots alarm lead time: for the seven confirmed deformation events, median lead time over the manual inspection trigger was 11 days, with an interquartile range of 7–16 days. The workload is compatible with post-shift processing on a standard workstation [31]. Practical deployment should retain independent geotechnical inspection [32] and site-specific threshold validation [33].

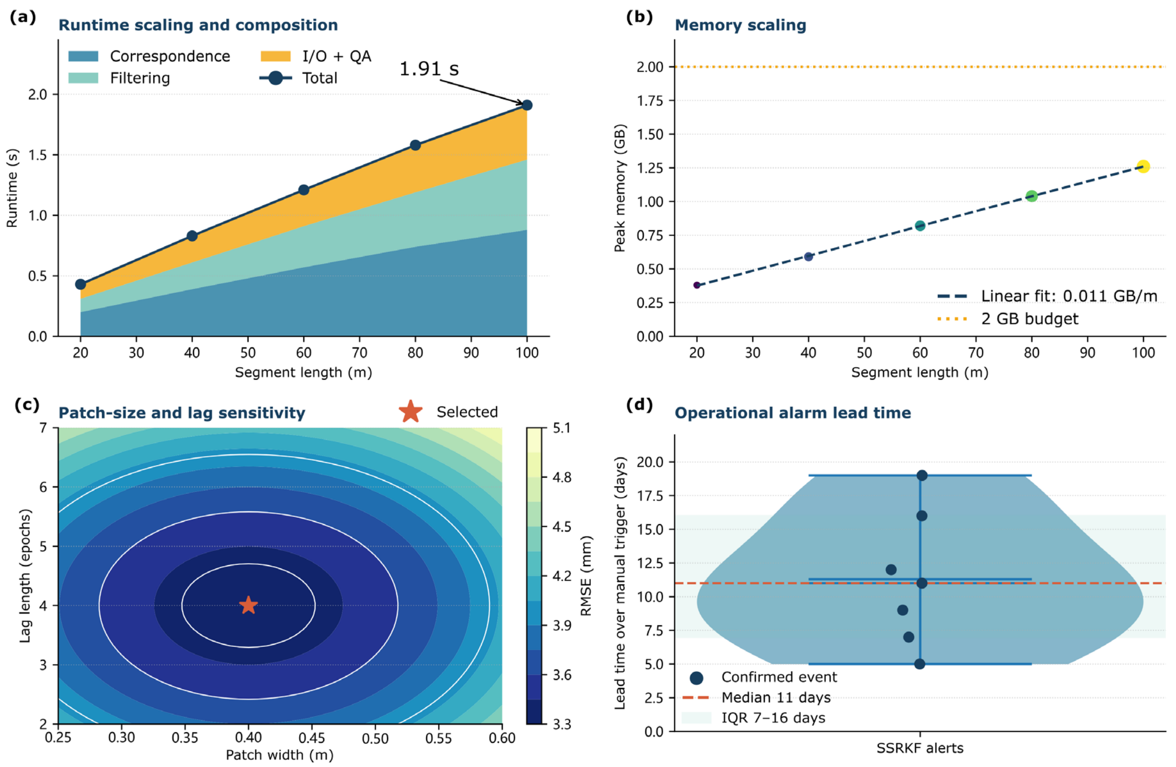

Figure 7. Deployment characteristics: (a) runtime scaling; (b) memory scaling; (c) patch-size sensitivity; (d) alarm lead-time distribution for confirmed events.

Operational Interpretation

The posterior field will serve as the filter and is not required to be a complete ground-control decision-making entity. A wide-spread offset across the entire area and an increase in bias estimation indicate alignment degradation, whereas a small cluster with a consistent normal direction and rate is more consistent with structural movement. Uncertainty Maps show areas that would be better dealt with by re-scanning rather than immediately escalated. In the test campaigns, 78% of the rejected patches were due to mesh occlusion, water

https://doi.org/10.64972/dea.2023.v2i1.2942d:16-27

glare or overlap less than 45%, and most were recovered after the next scan. Each alert is tracked to accept observations, innovative weights, neighboring support, and fixed delay corrections.

The experiment has also set the scope of the model. Motions of 3 mm or less were often indistinguishable from reference uncertainty, and coherent changes of more than 5 mm had a median absolute error of 2.4 mm. Therefore, the way is suitable for repeated screening and trend observation, but not for sub-millimeter-scale crack-aperture metrology. The calibrated interval is relatively small near the 10mm action threshold; a deterministic map would be more precise than the support provided by a scan.

A tier resurvey schedule can be generated from the deformation field for the normal installation. Stable sections with a small uncertainty range are included in the normal campaign cycle. A spatially coherent watch cluster is assigned an earlier scan, and a watch generated mainly by broad uncertainty is first examined for trajectory coverage, dust conditions, wet surfaces and anchor availability. Otherwise, these poor-quality scans will be regarded as validly confirmed. The recommended re-scan should change at least one weak geometric factor, for example, by reducing vehicle speed, altering the scanner offset, or adding a short stationary scan. The following observations will provide new evidence for the state estimation.

Engineering interpretation should also consider the spatial form of the estimated movement. A narrow peak next to a bolt plate may be caused by local correspondence instability, and a continuous band across several roof patches is more typical of sag or bedding separation. Movement in both the roof and at the nominally stable anchors indicates that registration needs to be revised before concluding that it is a structural issue. Therefore, the diagnostic records will be sent along with each monitoring and alert. The record will log the history of deviations, observation acceptance rates, neighborhood support, and uncertainty width. These quantities are not replacements for geotechnical judgment, but they make the basis of the automatic status visible and enable engineers to distinguish a credible deformation trend from a survey-quality problem before arranging inspections or support measures.

Conclusion

This paper proposes a state-space refined Kalman filter for detecting roadway-roof deformation based on multiple underground LiDAR scans. The model distinguishes between structural displacement and registration bias, adjusts measurement uncertainty to accommodate scanning geometry and innovative behavior, rejects contaminated observations through bounded gate control, and improves recent estimates through fixed lag backpropagation. A roof-aligned patch observation and probability-based alarm rule connect the estimator to deployable monitoring practice.

Currently, the implemented solution still assumes that stable sidewall and floor anchors are available in each section. Very rapid collapse processes cannot be represented by the smooth dynamic model, and dense meshes or water films may leave too little roof surface for a defendable update. Only one mining environment and a limited number of scanner trajectories have been included in the evaluation; thus, threshold portability and long-term sensor ageing have not been fully tested.

Future work will connect the bias state of adjacent trajectory segments, introduce change-point dynamics for abrupt events, and test transfer across different lithologies, support systems and scanners. Incorporate geotechnical stress indicators and automatic rescheduling of re-scans to improve the timeliness of decision-making further, and retain the open-book uncertainty accounting necessary for safety-critical applications.

Author Contributions

Hamdan Al-Suwaidi contributes to conceptualization, methodology, software, validation, analysis, investigation, data collection, draft preparation, manuscript editing, visualization, supervision, project administration, and funding acquisition. Zainab Al-Zaabi, Amal Al-Hashimi and Mishaala Al-Tunaiji contribute to validation, analysis, investigation, data collection, draft preparation. All authors have read and agreed with the manuscript before its submission and publication.

Funding

This research received no specific financial support from any funding agency.

Institutional Review Board Statement

Not applicable.

References

[1] Xiang, J. (2022). Research on deformation monitoring of tunnel engineering based on 3D laser scanning. Applied Mathematics and Nonlinear Sciences, 8(2), 513-528. https://doi.org/10.2478/amns.2021.2.00204

[2] Jiang, Q., Zhong, S., Pan, P. Z., Shi, Y., Guo, H. G. & Kou, Y. (2020). Observe the temporal evolution of deep tunnel's 3D deformation by 3D laser scanning in the Jinchuan No. 2 Mine. Tunnelling and Underground Space Technology, 97, 103237-103237. https://doi.org/10.1016/j.tust.2019.103237

[3] Janus, J. & Ostrogórski, P. (2022). Underground Mine Tunnel Modelling Using Laser Scan Data in Relation to Manual Geometry Measurements. Energies, 15(7), 2537-2537. https://doi.org/10.3390/en15072537

[4] Ge, Y., Tang, H., Gong, X., Zhao, B., Lü, Y., Chen, Y., ... & Qiu, Y. (2019). Deformation Monitoring of Earth Fissure Hazards Using Terrestrial Laser Scanning. Sensors, 19(6), 1463-1463. https://doi.org/10.3390/s19061463

[5] Kalenjuk, S., Lienhart, W. & Rebhan, M. (2021). Processing of mobile laser scanning data for large-scale deformation monitoring of anchored retaining structures along highways. Computer-Aided Civil and Infrastructure Engineering, 36(6), 678-694. https://doi.org/10.1111/mice.12656

[6] Fahle, L., Holley, E., Walton, G., Petruska, A. J. & Brune, J. F. (2022). Analysis of SLAM-Based Lidar Data Quality Metrics for Geotechnical Underground Monitoring. Mining Metallurgy & Exploration, 39(5), 1939-1960. https://doi.org/10.1007/s42461-022-00664-3

[7] Jia, D., Zhang, W., Wang, Y. & Liu, Y. (2021). A New Approach for Cylindrical Steel Structure Deformation Monitoring by Dense Point Clouds. Remote Sensing, 13(12), 2263-2263. https://doi.org/10.3390/rs13122263

[8] Gómez, J., Casas, J. R. & Villalba, S. (2020). Structural Health Monitoring with Distributed Optical Fiber Sensors of tunnel lining affected by nearby construction activity. Automation in Construction, 117, 103261-103261. https://doi.org/10.1016/j.autcon.2020.103261

[9] Baek, J., Park, J., Cho, S. & Lee, C. W. (2022). 3D Global Localization in the Underground Mine Environment Using Mobile LiDAR Mapping and Point Cloud Registration. Sensors, 22(8), 2873-2873. https://doi.org/10.3390/s22082873

[10] Zováthi, Ö., Nagy, B. & Benedek, C. (2022). Point cloud registration and change detection in urban environment using an onboard Lidar sensor and MLS reference data. International Journal of Applied Earth Observation and Geoinformation, 110, 102767-102767. https://doi.org/10.1016/j.jag.2022.102767

[11] Zhu, B., Ye, Y., Zhou, L., Li, Z. & Yin, G. (2021). Robust registration of aerial images and LiDAR data using spatial constraints and Gabor structural features. ISPRS Journal of Photogrammetry and Remote Sensing, 181, 129-147. https://doi.org/10.1016/j.isprsjprs.2021.09.010

[12] Zang, Y., Yang, B., Li, J. & Guan, H. (2019). An Accurate TLS and UAV Image Point Clouds Registration Method for Deformation Detection of Chaotic Hillside Areas. Remote Sensing, 11(6), 647-647. https://doi.org/10.3390/rs11060647

[13] Sharifisoraki, Z., Dey, A., Selzler, R., Amini, M., Green, J. R., Rajan, S. & Kwamena, F. (2022). Monitoring Critical Infrastructure Using 3D LiDAR Point Clouds. IEEE Access, 11, 314-336. https://doi.org/10.1109/access.2022.3232338

[14] Huang, R., Xu, Y., Yao, W., Hoegner, L. & Stilla, U. (2020). Robust global registration of point clouds by closed-form solution in the frequency domain. ISPRS Journal of Photogrammetry and Remote Sensing, 171, 310-329. https://doi.org/10.1016/j.isprsjprs.2020.11.014

[15] Dunn, M., Reid, P. & Malos, J. (2020). Development of a Protective Enclosure for Remote Sensing Applications—Case Study: Laser Scanning in Underground Coal Mines. Resources, 9(5), 56-56. https://doi.org/10.3390/resources9050056

[16] Kütimets, K., Ellmann, A., Väli, E. & Kanter, S. (2021). Underground oil shale mine surveying using handheld mobile laser scanners. Oil Shale, 38(1), 42-64. https://doi.org/10.3176/oil.2021.1.03

[17] Nielsen, K. & Hendeby, G. (2022). Survey on 2D Lidar Feature Extraction for Underground Mine Usage. IEEE Transactions on Automation Science and Engineering, 20(2), 981-994. https://doi.org/10.1109/tase.2022.3172522

[18] Xiao, Y., Yang, C., Li, J., Zhou, K., Lin, Y. & Sun, G. (2022). Estimation of the Mean Trace Length of Discontinuities in an Underground Drift Using Laser Scanning Point Cloud Data. Sustainability, 14(23), 15650-15650. https://doi.org/10.3390/su142315650

[19] Huang, M., Wei, Z., Zhao, J., Jabr, R. A., Pau, M. & Sun, G. (2019). Robust Ensemble Kalman Filter for Medium-Voltage Distribution System State Estimation. IEEE Transactions on Instrumentation and Measurement, 69(7), 4114-4124. https://doi.org/10.1109/tim.2019.2945743

[20] Wang, Y., Sun, Y., Dinavahi, V., Cao, S. & Hou, D. (2019). Adaptive Robust Cubature Kalman Filter for Power System Dynamic State Estimation Against Outliers. IEEE Access, 7, 105872-105881. https://doi.org/10.1109/access.2019.2932261

[21] Li, Y., Li, J., Qi, J. & Chen, L. (2019). Robust Cubature Kalman Filter for Dynamic State Estimation of Synchronous Machines Under Unknown Measurement Noise Statistics. IEEE Access, 7, 29139-29148. https://doi.org/10.1109/access.2019.2900228

[22] Hu, G., Gao, B., Zhong, Y. & Gu, C. (2020). Unscented kalman filter with process noise covariance estimation for vehicular ins/gps integration system. Information Fusion, 64, 194-204. https://doi.org/10.1016/j.inffus.2020.08.005

[23] Chiella, A. C. B., Teixeira, B. O. S. & Pereira, G. A. S. (2019). Quaternion-Based Robust Attitude Estimation Using an Adaptive Unscented Kalman Filter. Sensors, 19(10), 2372-2372. https://doi.org/10.3390/s19102372

[24] He, J., Sun, C., Zhang, B. & Wang, P. (2020). Variational Bayesian-Based Maximum Correntropy Cubature Kalman Filter With Both Adaptivity and Robustness. IEEE Sensors Journal, 21(2), 1982-1992. https://doi.org/10.1109/jsen.2020.3020273

[25] Wang, L., Ma, J., Zhao, X., Li, X., Zhang, K. & Jiao, Z. (2022). Adaptive robust unscented Kalman filter-based state-of-charge estimation for lithium-ion batteries with multi-parameter updating. Electrochimica Acta, 426, 140760-140760. https://doi.org/10.1016/j.electacta.2022.140760

[26] Youn, W. & Gadsden, S. A. (2019). Combined Quaternion-Based Error State Kalman Filtering and Smooth Variable Structure Filtering for Robust Attitude Estimation. IEEE Access, 7, 148989-149004. https://doi.org/10.1109/access.2019.2946609

[27] Yang, B., Huang, H. Q. & Cao, L. (2022). Centered Error Entropy-Based Sigma-Point Kalman Filter for Spacecraft State Estimation with Non-Gaussian Noise. Space Science & Technology, 2022, 9854601. https://doi.org/10.34133/2022/9854601

[28] Liu, Z. & Chan, S. C. (2020). Adaptive Fading Bayesian Unscented Kalman Filter and Smoother for State Estimation of Unmanned Aircraft Systems. IEEE Access, 8, 119470-119486. https://doi.org/10.1109/access.2020.3004804

[29] Pointon, H. A. G., McLoughlin, B. J., Matthews, C. & Bezombes, F. (2019). Towards a Model Based Sensor Measurement Variance Input for Extended Kalman Filter State Estimation. Drones, 3(1), 19-19. https://doi.org/10.3390/drones3010019

[30] Hu, C., Yang, X., Huang, R. & Ma, X. (2020). Presplitting Blasting the Roof Strata to Control Large Deformation in the Deep Mine Roadway. Advances in Civil Engineering, 2020(1), 8886991. https://doi.org/10.1155/2020/8886991

[31] Ma, Z., Liang, X., Fu, G., Zou, Y., Chen, A. & Guan, R. (2021). Experimental and numerical investigation of energy dissipation of roadways with thick soft roofs in underground coal mines. Energy Science & Engineering, 9(3), 434-446. https://doi.org/10.1002/ese3.832

[32] Sun, Y., Bi, R., Sun, J., Zhang, J., Taherdangkoo, R., Huang, J. & Li, G. (2022). Stability of roadway along hard roof goaf by stress relief technique in deep mines: a theoretical, numerical and field study. Geomechanics and Geophysics for Geo-Energy and Geo-Resources, 8(2), s40948-022-00356-8. https://doi.org/10.1007/s40948-022-00356-8

[33] Hao, J., Li, X., Song, Y., Zhang, P. & Liu, H. (2021). Analysis of mining roadway with large deformation of broken soft coal and research on supporting technology: A case study in Xin'an coal mine, China. Engineering Failure Analysis, 130, 105761. https://doi.org/10.1016/j.engfailanal.2021.105761